

# Further Sunyaev–Zel’dovich observations of two *Planck* ERCSC clusters with the Arcminute Microkelvin Imager<sup>\*</sup>

AMI Consortium: Natasha Hurley-Walker<sup>1</sup>†, Michael L. Brown<sup>1,2</sup>, Matthew L. Davies<sup>1</sup>, Farhan Feroz<sup>1</sup>, Thomas M. O. Franzen<sup>3</sup>, Keith Grainge<sup>1,2</sup>, Michael P. Hobson<sup>1</sup>, Anthony Lasenby<sup>1,2</sup>, Malak Olamaie<sup>1</sup>, Guy Pooley<sup>1</sup>, Carmen Rodríguez-Gonzálvez<sup>1</sup>, Richard D. E. Saunders<sup>1,2</sup>, Michel P. Schammel<sup>1</sup>, Anna M. M. Scaife<sup>4</sup>, Paul F. Scott<sup>1</sup>, Timothy Shimwell<sup>1</sup>, David Titterton<sup>1</sup> and Elizabeth Waldram<sup>1</sup>

<sup>1</sup> *Astrophysics Group, Cavendish Laboratory, 19 J. J. Thomson Avenue, Cambridge CB3 0HE*

<sup>2</sup> *Kavli Institute for Cosmology, Cambridge, Madingley Road, Cambridge CB3 0HA*

<sup>3</sup> *CSIRO Astronomy & Space Science, PO Box 76, Epping, NSW 1710, Australia*

<sup>4</sup> *Dublin Institute for Advanced Studies, 31 Fitzwilliam Place, Dublin 2, Ireland*

Accepted —; received —; in original form 12 November 2021

## ABSTRACT

We present follow-up observations of two galaxy clusters detected blindly via the Sunyaev-Zel’dovich (SZ) effect and released in the *Planck* Early Release Compact Source Catalogue. We use the Arcminute Microkelvin Imager, a dual-array 14–18 GHz radio interferometer. After radio source subtraction, we find a SZ decrement of integrated flux density  $-1.08 \pm 0.10$  mJy toward PLCKESZ G121.11+57.01, and improve the position measurement of the cluster, finding the centre to be RA  $12^{\text{h}} 59^{\text{m}} 36.4^{\text{s}}$ , Dec  $+60^{\circ} 04' 46'' 8$ , to an accuracy of  $20''$ . The region of PLCKESZ G115.71+17.52 contains strong extended emission, so we are unable to confirm the presence of this cluster via the SZ effect.

**Key words:** cosmology: observations – radiation mechanisms: non-thermal – cosmic microwave background – galaxies: clusters – Sunyaev-Zel’dovich – galaxies: clusters: individual (PLCKESZ G115.71+17.52, PLCKESZ G121.11+57.01)

## 1 INTRODUCTION

The *Planck* satellite is an instrument designed to measure the full Cosmic Microwave Background (CMB) sky to the highest sensitivity yet achieved. Part of its remit is a blind survey of galaxy clusters via their Sunyaev-Zel’dovich effects (SZ; Sunyaev & Zel’dovich 1970); this occurs when CMB photons are inverse-Compton scattered by hot gas in galaxy clusters. The resulting shift in the blackbody spectrum of the CMB produces a decrement at radio frequencies below the null of 217 GHz and a positive signal above this frequency (see e.g. Birkinshaw (1999) and Carlstrom et al. (2002) for reviews).

The Arcminute Microkelvin Imager (AMI) is a dual-array radio interferometer operating at 14–18 GHz; part of its scientific programme is making observations of hundreds of known galaxy clusters to measure their gas masses and structures. Along with its high sensitivity, its resolution of  $\simeq 2.5'$  allows the measurement of

the extent and shape of galaxy clusters above a redshift of  $\simeq 0.1$  (below which they become resolved out).

In 2011, the *Planck* Early Release Compact Source Catalogue (ERCSC; Planck Collaboration 2011b) was made publicly available; it includes a sample of 189 galaxy clusters detected via their SZ effects at signal-to-noise (S/N)  $> 6$  (Planck Collaboration 2011a). AMI was used to follow up the two previously unconfirmed clusters lying in the northern sky: PLCKESZ G115.71+17.52 (S/N = 6.78) and PLCKESZ G121.11+57.01 (S/N = 6.66), AMI observing details of which can be found in Tab. 1.

## 2 AMI SZ OBSERVATIONS

AMI comprises two aperture synthesis arrays located at the Mullard Radio Astronomy Observatory, Lord’s Bridge, Cambridge, UK. The AMI Small Array (SA) consists of ten 3.7-m diameter equatorially-mounted dishes with a baseline range of  $\simeq 5$ –20 m, while the AMI Large Array (LA) has eight 12.8-m-diameter dishes with a baseline range of  $\simeq 20$ –100 m. Both arrays observe I+Q in the band 14–18 GHz, each with system temperatures of about 25 K.

<sup>\*</sup> We request that any reference to this paper cites “AMI Consortium: Hurley-Walker et al. 2011”

† Issuing author; E-mail: nh313@mrao.cam.ac.uk

Name	RA (J2000)	Dec (J2000)	SA observing time / hrs	SA map noise / $\mu\text{Jy beam}^{-1}$	LA observing time / hrs	LA 19-pt map noise/ $\mu\text{Jy beam}^{-1}$	LA 61-pt map noise/ $\mu\text{Jy beam}^{-1}$
PLCKESZ G115.71+17.52	22 26 24.9	+78 18 15.8	50	78	77	55	200
PLCKESZ G121.11+57.01	12 59 23.8	+60 05 24.8	40	81	67	65	250

**Table 1.** Statistics of the AMI observations of the two candidates.

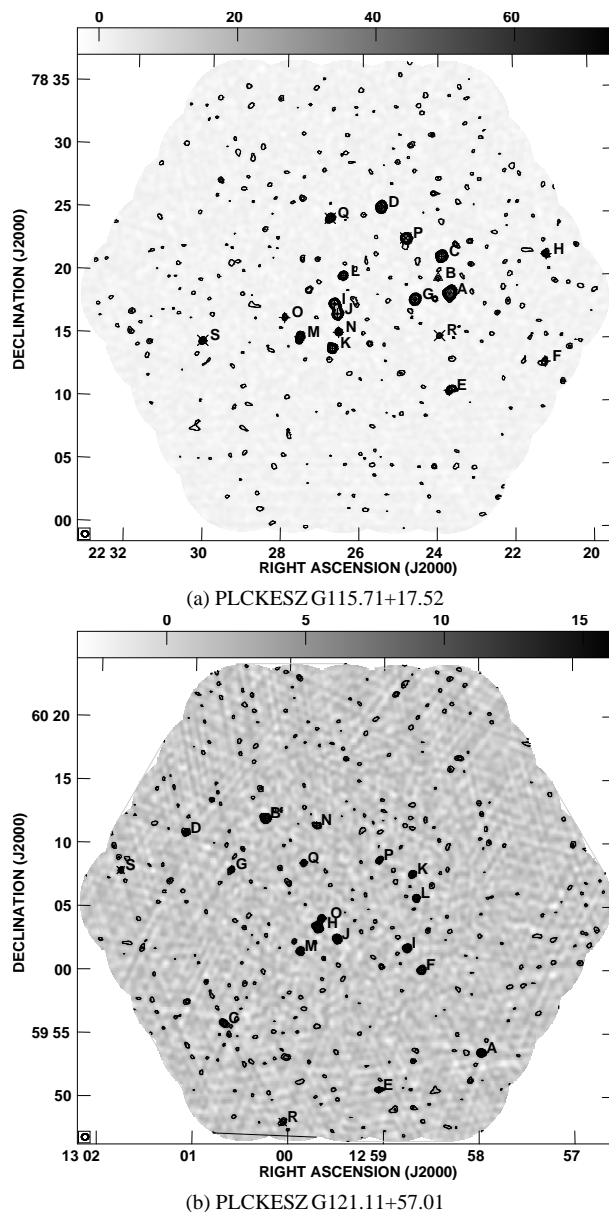
Channel	$\nu/\text{GHz}$	$S^{3\text{C}286}/\text{Jy}$	$S^{3\text{C}48}/\text{Jy}$	$\text{FWHM}_{\text{LA}}/''$
3	13.9	3.74	1.89	6.08
4	14.6	3.60	1.78	5.89
5	15.3	3.47	1.68	5.70
6	16.1	3.35	1.60	5.53
7	16.9	3.24	1.52	5.39
8	17.6	3.14	1.45	5.25

**Table 2.** Assumed I+Q flux densities of 3C286 and 3C48 over the commonly-used AMI band, and the LA primary beam full-width-half-maxima (FWHM) for each channel.

The backends are analogue Fourier transform spectrometers, from which the complex signals in each of eight channels of 750-MHz bandwidth are synthesised, and the signals in the synthesised channels are correlated at the  $\simeq 10$  per cent level. In practice, the two lowest-frequency channels are generally not used due to a poor correlator response in this frequency range and interference from geostationary satellites. Further telescope details are given in AMI Consortium: Zwart et al. (2008).

The AMI data reduction was performed using our in-house reduction software REDUCE. This is used to apply path-compensator and path-delay corrections, to flag interference, shadowing and hardware errors, to apply phase and amplitude calibrations, make a correction for the changing intervening air mass and to Fourier transform the correlator data to synthesise the frequency channels, before outputting to disk in *uv*-FITS format suitable for imaging in the Astronomical Image Processing System (AIPS; Astronomical Image Processing Software 2007). Flux calibration was performed using short observations of 3C48 and 3C286 near the beginning and end of each run, with assumed I+Q flux densities for these sources in the AMI channels consistent with Baars et al. (1977) (see Tab. 2). As Baars et al. measure I and AMI measures I+Q, these flux densities include corrections for the polarization of the sources. The phase calibrators, J0017+8135, J1302+5748 and J2133+8239, were chosen from the Jodrell Bank VLA Survey (JVAS; Patnaik et al. 1992) on the basis of proximity ( $\leq 5^\circ$ ) and flux density ( $\geq 0.7$  Jy at 15 GHz). After phase calibration, the phase of AMI over one hour is generally stable to  $5^\circ$  for channels 4–7, and to  $10^\circ$  for channels 3 and 8. The overall consistency of the flux-density scale is estimated to be better than five per cent.

To analyse the SA cluster observations we use a Bayesian analysis package, MCADAM (Marshall et al. 2003 and Feroz et al. 2009b). This uses MULTINEST (Feroz & Hobson 2008 and Feroz et al. 2009a), an implementation of nested sampling (Skilling 2004), to efficiently explore the multidimensional parameter space and to calculate the Bayesian evidence. This analysis has been applied to pointed observations of known clusters (e.g. AMI Consortium: Rodríguez-González et al. 2010; AMI Consortium: Zwart et al. 2010), and also to detect previously unknown clusters (AMI Consortium: Shimwell et al. 2010). We use it here to model the effect of radio point sources on the SA data, using the LA data as priors. To transform the SA data into a format suitable for MCADAM, the *uv*-data for all good observations were concatenated together to make a *uv*-FITS file for each channel. These were then transformed into lists of visibilities for the purpose of generating a co-

**Figure 1.** LA raster signal-to-noise maps of the two candidates, with sources detected at  $4\sigma$  and above marked; their properties can be found in Tables 3 and 4. Contours are  $S/N=1$ , and follow levels +3, +4, +5, +6, +8, +10 and +20. The small ellipse in the box in the lower-left shows the average synthesised beam.

variance matrix for the data. The covariance matrix describes the terms which contribute to the data but are not part of the model, i.e. the CMB, thermal noise from the telescope and confusion noise from unresolved point sources. The latter were modelled using the Tenth Cambridge Radio Survey (10C: AMI Consortium: Franzen

et al. 2010; AMI Consortium: Davies et al. 2010), integrating the confusion power from zero up to the LA source detection limit.

The data were also binned into cells of width  $40\lambda$ , determined in Marshall (2003) as a suitable binning scale to reduce the size of the data to a manageable level without adversely affecting the resulting inference of model parameters. The binned data files were then analysed by MCADAM using the method described in AMI Consortium: Zwart et al. (2010). Maps were made using IMAGR in AIPS from each channel of the SA and LA observations; however we here present only the combined-channel maps of the SA and LA observations. The task `imean` was used on the LA individual maps to attach the map noise to the map header, and `flatn` was then used to stitch the maps together, with a primary beam correction applied using parameters shown in Tab. 2.

Source-finding was carried out on the LA data using software modified from that used in the 9C survey (Waldram et al. 2003). Spectral indices were fitted using LA maps of all six channels, assuming source fluxes follow a power-law relation of  $S \propto \nu^{-\alpha}$  for the AMI frequencies. The properties of point sources detected at  $4\sigma$  and above by the LA are used as priors when modelling the SA data in MCADAM. The position prior used in MCADAM is a delta function since the resolution of the LA is around three times that of the SA; two exceptions are discussed in Section 3.1. LA flux densities generated the peak of Gaussian priors on the SA source flux densities, with  $\sigma$ s set to the calibration error of five per cent of the source flux density added in quadrature with the local map noise. Spectral index ( $\alpha$ ) priors were also set as Gaussians with  $\sigma$  equal to the error on the spectral index fit. These errors tend to be small ( $\simeq 0.4$ ) for bright sources and large ( $\simeq 2$ ) for faint sources. Fig. 1 shows the LA maps for the candidates with  $4\sigma_{\text{LA}}$  radio point sources marked; the positions and properties of the sources are given in Tables 3 and 4.

### 3 RESULTS AND DISCUSSION

After the source models were fitted to the SA data in MCADAM, the sources were subtracted from the data using the modelled source fluxes and spectral indices. The data were then mapped again in AIPS to generate source-subtracted maps. The parameters used for source-subtraction are the last two columns of Tables 3 and 4.

#### 3.1 PLCKESZG115.71+17.52

The raw map for this candidate, Fig. 2a, shows a very complicated region with both positive and negative features. The sources appear to consist of two main complexes: one to the south-east of the pointing centre, consisting of sources L, I, J, N, K, M and O. To the west and north is a separate complex, consisting of sources D, P, C, B, G and the extended source A. Given the extent of this source, and the uncertainty on whether source B was also extended, these were modelled with Gaussian position priors with  $\sigma = 5''$ . This is useful when dealing with extended emission as the location and magnitude of the peak of such emission may differ significantly when measured on different scales; it has previously been used to account for small amounts of extended emission in AMI Consortium: Shimwell et al. (2011) and AMI Consortium: Rodríguez-González et al. (2011).

After source-subtraction (see Fig. 2b), extended positive residuals are visible directly to the north of the pointing centre, and to the south of source A. These areas of emission have no obvious counterparts on the LA map (Fig. 1a) and have SA peak flux densities

$\simeq 0.4$  mJy. However the complexes have integrated flux densities of  $\simeq 0.7$  mJy each. This seems to indicate that the emission is real, extended, and positive.

A difficulty arises when using an interferometer to measure structure of unknown extent, as it is unclear how much will be resolved out due to the lack of  $uv$ -coverage on large scales. This partially negates the natural filtering advantage of using an interferometer for SZ detection, discussed in Birkinshaw (1999). When deconvolving the dirty map with the synthesised beam in the CLEAN process (Clark 1980), incomplete interferometric measurement of extended structure can lead to artifacts, including negative signal. It is unclear whether the negative signal  $7'$  south-west of the pointing centre, in the source-subtracted map, is purely artifactual from poor CLEANing of the extended positive emission, or also includes a component from SZ emission. Publicly available *ROSAT* data (Voges et al. 1999) show elongated X-ray emission of  $\simeq 5'$  extent at the *Planck* ESZ position. If this object is a galaxy cluster then the SZ and X-ray emission are likely not to be strongly offset, so the south-west negative feature (and other negative features on the map) are probably artifactual.

As to the source of the positive extended emission seen in this region, we note that Galactic observations with the SA (see e.g. AMI Consortium: Hurley-Walker et al. 2009) tend to pick up more extended emission closer to the Galactic plane. This is likely to be synchrotron associated with regions which also have bright thermal dust emission. The latter was also noted by Planck Collaboration (2011a) as a problem when measuring the SZ effect toward this object. There is also the possibility that the two source complexes are extended radio doubles from jet-producing galaxies, which would be more likely to appear in a galaxy cluster than in the field.

#### 3.2 PLCKESZG121.11+57.01

It is clear even before source subtraction that there is isolated excess negative signal in the centre of the SA map, Fig. 3a. After source-subtraction the initially elliptical appearance is revealed as a close to circularly-symmetric SZ decrement, Fig. 3b. The  $6\sigma$  positive residual between sources P and N corresponds well to an overdensity of  $3\sigma$  features nearby in the LA map, and is likely to be extended emission resolved-out by the LA. The feature is more than one synthesised beam away from the cluster and appears alone, so should not affect measurement of the cluster decrement.

From the source-subtracted map, we measure the integrated flux density of the central negative signal as  $-1.08 \pm 0.10$  mJy. We estimate the S/N of our measurement as 13, by dividing the absolute value of the integrated flux density by the map noise of  $0.081$  mJy. Thus we confirm the *Planck* blind SZ detection of PLCKESZG121.11+57.01 as a galaxy cluster. We hope to investigate the full comparison of AMI and Planck data via common cluster models in future publications.

We also measure a position offset from the ERCSC position, finding  $\Delta_{\text{RA}} = +94 \pm 13''$  and  $\Delta_{\text{Dec}} = -38 \pm 19''$ , resulting in an improved cluster position of RA  $12^{\text{h}} 59^{\text{m}} 36.4^{\text{s}}$ , Dec  $+60^{\circ} 04' 46.8''$ . Wen et al. (2009) identify a cluster of redshift 0.33 at RA  $12^{\text{h}} 59^{\text{m}} 33.4^{\text{s}}$ , Dec  $+60^{\circ} 04' 09''$  in the Sloan Digital Sky Survey DR6 Galaxy Clusters Catalog. Given that the separation between these two measurements is merely  $44''$ , and the redshift is typical of clusters detected by *Planck* (Planck Collaboration 2011a), it is likely that the two are the same object. Publicly-available *ROSAT* data (Voges et al. 1999) show only a few X-ray photons, consistent with noise, so the cluster appears to have a low X-ray luminosity.

ID	RA	Dec	$S_{LA}/mJy$	$\alpha_{LA}$	$S_{MCADAM}/mJy$	$\alpha_{MCADAM}$
A	22 23 41.0	+78 18 35.1	$6.73 \pm 0.83$	$0.55 \pm 0.21$	$8.71 \pm 0.09$	$0.79 \pm 0.11$
B	22 23 59.3	+78 19 49.4	$0.50 \pm 0.23$	$0.48 \pm 1.55$	$0.50 \pm 0.09$	$0.41 \pm 1.27$
C	22 23 53.6	+78 21 29.1	$3.64 \pm 0.61$	$0.43 \pm 0.45$	$4.32 \pm 0.08$	$0.68 \pm 0.19$
D	22 25 29.4	+78 25 25.3	$2.53 \pm 0.51$	$0.89 \pm 0.53$	$2.47 \pm 0.08$	$1.14 \pm 0.28$
E	22 23 41.6	+78 10 51.1	$2.02 \pm 0.40$	$1.14 \pm 1.58$	$2.18 \pm 0.12$	$2.13 \pm 0.60$
F	22 21 12.6	+78 13 08.6	$1.75 \pm 0.61$	$-0.99 \pm 1.77$	$1.03 \pm 0.35$	$-1.16 \pm 1.68$
G	22 24 35.3	+78 18 05.5	$1.67 \pm 0.41$	$2.13 \pm 0.61$	$1.80 \pm 0.07$	$1.25 \pm 0.33$
H	22 21 09.2	+78 21 40.8	$1.37 \pm 0.47$	$0.37 \pm 1.73$	$1.63 \pm 0.23$	$1.56 \pm 1.13$
I	22 26 41.7	+78 17 39.7	$1.14 \pm 0.34$	$0.74 \pm 0.70$	$1.16 \pm 0.09$	$1.67 \pm 0.39$
J	22 26 36.9	+78 16 53.3	$1.12 \pm 0.34$	$0.28 \pm 0.72$	$1.35 \pm 0.09$	$0.97 \pm 0.39$
K	22 26 43.9	+78 14 08.0	$0.82 \pm 0.29$	$0.63 \pm 1.01$	$0.74 \pm 0.07$	$0.04 \pm 0.74$
L	22 26 28.4	+78 19 55.8	$0.77 \pm 0.28$	$-0.23 \pm 1.01$	$0.09 \pm 0.05$	$-0.01 \pm 0.98$
M	22 27 34.7	+78 15 00.6	$0.72 \pm 0.28$	$0.25 \pm 1.04$	$0.91 \pm 0.07$	$0.13 \pm 0.81$
N	22 26 34.7	+78 15 24.9	$0.31 \pm 0.18$	$1.15 \pm 1.56$	$0.41 \pm 0.06$	$0.90 \pm 1.38$
O	22 27 59.3	+78 16 31.5	$0.28 \pm 0.18$	$0.90 \pm 1.70$	$0.16 \pm 0.06$	$0.73 \pm 1.62$
P	22 24 50.3	+78 22 57.7	$2.06 \pm 0.42$	$0.30 \pm 0.73$	–	–
Q	22 26 49.9	+78 24 28.7	$0.53 \pm 0.27$	$0.70 \pm 1.37$	–	–
R	22 23 56.9	+78 15 12.8	$0.47 \pm 0.23$	$0.23 \pm 1.66$	–	–
S	22 30 06.4	+78 14 34.4	$0.40 \pm 0.40$	$0.40 \pm 1.63$	–	–

**Table 3.** Sources found in the LA map of PLCKESZ G115.71+17.52, in order of modelling prior and LA flux density. Sources A and B were modelled with a Gaussian position prior of  $\sigma = 5''$  to make allowance for the extended emission detected in this area. Sources P, Q, R, and S were directly subtracted from the SA data to reduce the computational resources needed to model the sources in the centre.

ID	RA	Dec	$S_{LA}/mJy$	$\alpha_{LA}$	$S_{MCADAM}/mJy$	$\alpha_{MCADAM}$
A	12 57 58.3	+59 53 32.9	$3.97 \pm 0.79$	$-1.08 \pm 1.35$	$2.91 \pm 0.37$	$-0.49 \pm 1.15$
B	13 00 15.4	+60 12 01.3	$2.66 \pm 0.55$	$0.20 \pm 0.95$	$2.55 \pm 0.13$	$-0.12 \pm 0.55$
C	13 00 40.7	+59 55 50.6	$2.47 \pm 0.61$	$0.22 \pm 1.46$	$3.26 \pm 0.24$	$0.52 \pm 0.84$
D	13 01 05.9	+60 10 49.4	$1.76 \pm 0.58$	$-1.04 \pm 1.63$	$1.13 \pm 0.23$	$-0.02 \pm 1.47$
E	12 59 03.0	+59 50 38.7	$1.71 \pm 0.57$	$-1.48 \pm 1.69$	$1.26 \pm 0.28$	$-1.68 \pm 1.55$
F	12 58 36.2	+60 00 04.8	$0.97 \pm 0.34$	$0.64 \pm 1.39$	$0.69 \pm 0.10$	$0.65 \pm 1.26$
G	13 00 36.8	+60 07 58.1	$0.85 \pm 0.35$	$-0.99 \pm 1.53$	$0.51 \pm 0.12$	$-0.92 \pm 1.39$
H	12 59 41.6	+60 03 25.2	$0.70 \pm 0.27$	$-0.17 \pm 1.13$	$0.74 \pm 0.12$	$1.27 \pm 0.75$
I	12 58 45.3	+60 01 49.0	$0.68 \pm 0.27$	$-1.54 \pm 1.37$	$0.58 \pm 0.09$	$-1.92 \pm 1.22$
J	12 59 29.6	+60 02 31.8	$0.64 \pm 0.26$	$-0.77 \pm 1.12$	$0.63 \pm 0.09$	$-0.25 \pm 0.95$
K	12 58 42.0	+60 07 39.5	$0.47 \pm 0.23$	$1.34 \pm 1.56$	$0.57 \pm 0.08$	$1.67 \pm 1.27$
L	12 58 39.6	+60 05 45.0	$0.46 \pm 0.23$	$0.46 \pm 1.66$	$0.32 \pm 0.08$	$0.66 \pm 1.48$
M	12 59 52.9	+60 01 33.2	$0.41 \pm 0.21$	$1.19 \pm 1.53$	$0.52 \pm 0.08$	$0.89 \pm 1.38$
N	12 59 42.9	+60 11 29.1	$0.38 \pm 0.21$	$0.68 \pm 1.75$	$0.48 \pm 0.09$	$0.09 \pm 1.47$
O	12 59 39.6	+60 04 08.9	$0.34 \pm 0.19$	$-1.22 \pm 1.64$	$0.34 \pm 0.09$	$-0.76 \pm 1.47$
P	12 59 03.1	+60 08 43.8	$0.29 \pm 0.18$	$-0.79 \pm 1.71$	$0.19 \pm 0.07$	$-0.51 \pm 1.64$
Q	12 59 51.2	+60 08 30.3	$0.28 \pm 0.18$	$-0.77 \pm 1.57$	$0.44 \pm 0.07$	$0.41 \pm 1.33$
R	13 00 03.2	+59 48 03.9	$4.68 \pm 1.35$	$-0.47 \pm 1.77$	–	–
S	13 01 46.8	+60 07 49.5	$3.66 \pm 1.04$	$-0.74 \pm 1.72$	–	–

**Table 4.** Sources found in the LA map of PLCKESZ G121.11+57.01, in order of modelling prior and LA flux density. Sources R and S were directly subtracted from the SA data to reduce the computational resources needed to model the sources in the centre.

## 4 CONCLUSIONS

We confirm the *Planck* blind SZ detection of PLCKESZ G121.11+57.01 as a galaxy cluster at  $13\sigma$ , with a 15 GHz integrated flux density of  $-1.08 \pm 0.10$  mJy. Our observations improve the measurement of the cluster position to RA  $12^h 59^m 36.4^s$ , Dec  $+60^\circ 04' 46''.8$ . We cannot positively identify PLCKESZ G115.71+17.52 as a galaxy cluster via SZ, as the data are consistent with both the presence of an SZ decrement and extended positive emission, or simply the latter. However we note that radio source environment may indicate the presence of jets from active galaxies, often found in galaxy clusters.

## 5 ACKNOWLEDGMENTS

We thank the staff of the Mullard Radio Astronomy Observatory for their invaluable assistance in the commissioning and operation of AMI, which is supported by Cambridge University and the STFC. Computational results were obtained using the COSMOS supercomputer (DiRAC STFC HPC Facility). This work was based on observations obtained with *Planck*, an ESA science mission with instruments and contributions directly funded by ESA Member States, NASA, and Canada. This research made

use of the *ROSAT* Data Archive of the Max-Planck-Institut für extraterrestrische Physik (MPE) at Garching, Germany. MLD, TMOF, CRG, MO, MPS and TWS acknowledge the support of PPARC/STFC studentships.

## REFERENCES

- AMI Consortium: Davies M. L., et al., 2010, ArXiv e-prints
- AMI Consortium: Franzen T. M. O., et al., 2010, ArXiv e-prints
- AMI Consortium: Hurley-Walker N., et al., 2009, MNRAS, 396, 365
- AMI Consortium: Rodríguez-González C., et al., 2010, ArXiv e-prints
- , 2011, ArXiv e-prints
- AMI Consortium: Shimwell T. W., et al., 2010, ArXiv e-prints
- , 2011, ArXiv e-prints
- AMI Consortium: Zwart J. T. L., et al., 2008, MNRAS, 391, 1545
- , 2010, ArXiv e-prints
- Astronomical Image Processing Software, 2007, [www.aips.nrao.edu](http://www.aips.nrao.edu)
- Baars J. W. M., Genzel R., Pauliny-Toth I. I. K., Witzel A., 1977, A&A, 61, 99
- Birkinshaw M., 1999, Phys.Rep., 310, 97

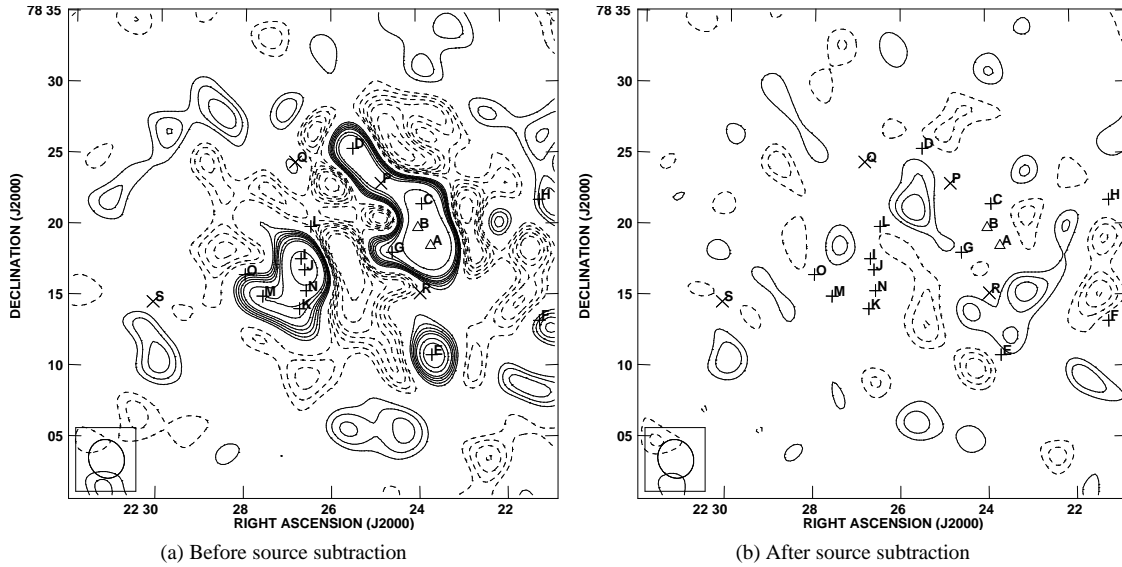


**Figure 2.** PLCKESZ G115.71+17.52 SA map before and after source subtraction; contours are every  $\sigma = 78\mu\text{Jy}$ , and follow levels  $-20, -10, -8, -6, -5, -4, -3, -2, +2, +3, +4, +5, +6, +8, +10$  and  $+20$ . Sources marked with a ‘+’ were modelled in MCADAM, while those marked with a ‘x’ were directly subtracted. The sources marked with a  $\Delta$  were given a Gaussian position priors of width  $5''$  due to their slightly extended structure. The parameters of the labelled sources can be found in Tab. 3. The small ellipse in the box in the lower-left shows the synthesised beam.

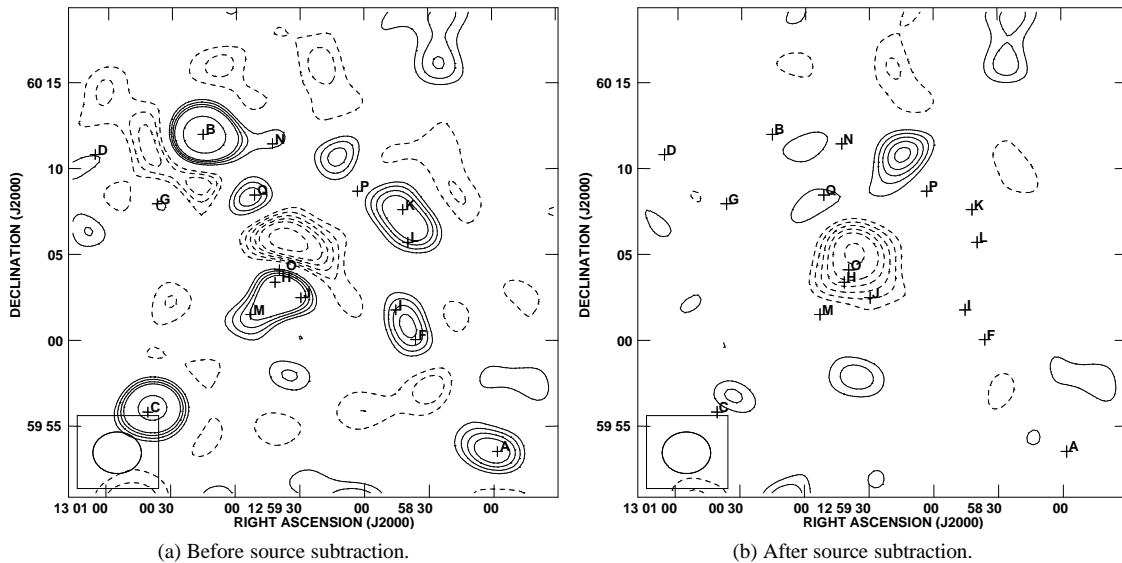


**Figure 3.** PLCKESZ G121.11+57.01 SA map before and after source subtraction; contours are every  $\sigma = 81\mu\text{Jy}$ , and follow the same levels as in Fig.2; annotations and markings are also the same. Sources E, R, and S are outside the field-of-view shown here, and the latter two were directly subtracted from the SA data. The parameters of the subtracted sources can be found in Tab. 4.

Carlstrom J. E., Holder G. P., Reese E. D., 2002, *ARA&A*, 40, 643

Clark B. G., 1980, *A&A*, 89, 377

Feroz F., Hobson M. P., 2008, *MNRAS*, 384, 449

Feroz F., Hobson M. P., Bridges M., 2009a, *MNRAS*, 398, 1601

Feroz F., Hobson M. P., Zwart J. T. L., Saunders R. D. E., Grainge K. J. B., 2009b, *MNRAS*, 398, 2049

Marshall P. J., 2003, PhD thesis, University of Cambridge

Marshall P. J., Hobson M. P., Slosar A., 2003, *MNRAS*, 346, 489

Patnaik A. R., Browne I. W. A., Wilkinson P. N., Wrobel J. M., 1992, *MNRAS*, 254, 655

Planck Collaboration, 2011a, ArXiv e-prints, 1101.2024

—, 2011b, ArXiv e-prints, 1101.2041

Skilling J., 2004, in *American Institute of Physics Conference Series*, Fischer R., Preuss R., Toussaint U. V., eds., pp. 395–405

Sunyaev R. A., Zeldovich Y. B., 1970, *Comments on Astrophysics and Space Physics*, 2, 66

Voges W., et al., 1999, *A&A*, 349, 389

Waldram E. M., Pooley G. G., Grainge K. J. B., Jones M. E., Saunders R. D. E., Scott P. F., Taylor A. C., 2003, *MNRAS*, 342, 915

Wen Z. L., Han J. L., Liu F. S., 2009, *ApJS*, 183, 197